Supporting Information

Elongated Fe-N-C containing trace atomic Co dopants for high power density PEMFCs

*Jiayao Cui [a,b], Junyong Min [a], Hao Wang [*a,c], Jianglan Shui [d], Lishan Peng [e], Zhenye Kang[f], Jieyuan Liu[d], Qingjun Chen [*e], Shuo Bai [a], Yanrong Liu [*a,b,c]*

a CAS Key Laboratory of Green Process and Engineering, State Key Laboratory of Mesoscience and Engineering, Beijing Key Laboratory of Ionic Liquids Clean Process, Institute of Process Engineering, Chinese Academy of Sciences, Beijing 100190, China.

b School of Chemical Engineering, University of Chinese Academy of Sciences, Beijing 100049, China

c Longzihu New Energy Laboratory, Zhengzhou Institute of Emerging Industrial Technology, Henan University, Zhengzhou 450000, China

d School of Materials Science and Engineering, Beihang University, Beijing, China

e Ganjiang Innovation Academy Chinese Academy of Sciences, Ganzhou 341000, China.

f State Key Laboratory of Marine Resource Utilization in South China Sea, Hainan Provincial Key Lab of Fine Chemistry, School of Chemical Engineering and Technology, Hainan University, Haikou 570228, China

Corresponding author E-mail address: haowang@ipe.ac.cn (Hao Wang); qjchen@ipe.ac.cn (Qingjun Chen); yrliu@ipe.ac.cn (Yanrong Liu)

1. Experimental Section:

1.1 Materials synthesis:

Preparation of Co-doped ZIF-8 (ZnCo-ZIF) precursor and Co-doped N-C (*t*Co-N-C) support. In a normal synthesis process, to obtain ZnCo-ZIF (Zn/Co 8:1) precursor, $Zn(NO_3)_2 \cdot 6H_2O$ (2.498 g) and $Co(NO_3)_2 \cdot 6H_2O$ (0.305 g) were dissolved in a conical flask containing 125 mL methanol (solution A). 2-methylimidazole (1.617 g) was dissolved in another conical flask containing 125 mL methanol (solution B). Then, the solution B was subsequently injected into solution A with thoroughly stirring for 24 h at 25°C. The as-obtained products were centrifuged and washed with methanol for several times and further dried in a vacuum oven at 70°C for overnight. The powder of ZnCo-ZIF precursor were transferred into a tube furnace and directly carbonized at 1100°C with a heating rate of 30 °C min^{-1} for 1 hour under constant nitrogen flow.

Preparation of Fe(*t*Co)-N-C catalysts. By using impregnation and adsorption strategy, controlled amounts of Fe^{3+} salts were anchored inside the pores of Co-doped N-C support (*t*Co-N-C). Firstly, a certain amount *t*Co-N-C powder was dispersed in an isopropanol solution containing ferric chloride. After a 2 hours ultrasonic dispersion and 2 hours magnetic stirring, the *t*Co-N-C+nFe^{3+} (n: the content of Fe^{3+} in the isopropanol solution, mg mL^{-1}) was obtained with a subsequently centrifugation and drying in a vacuum oven at 60°C overnight. Typically, to obtain Fe(*t*Co)-N-C, 60 mg *t*Co-N-C supports was dispersed in 6 mL isopropanol solution containing 4.5 mg $FeCl_3$ to prepare *t*Co-N-C+Fe^{3+} product. Subsequently, the impregnated support was placed in a tube furnace and thermal activated at 1000°C with a heating rate of 10 °C min^{-1}

under constant ammonia flow (100 mL min^{-1}) for 15 minutes.

1.2 Physical characterization:

The morphology of all prepared catalysts was observed by scanning electron microscope (SEM, Hitachi SU8020, 5 kV), transmission electron microscope (TEM, JEOL JEM-2100F, 200 kV) and high-angle annular dark-field scanning transmission electron microscope (HAADF-STEM, JEM-ARM300F, 300 kV). The crystal phases of the as-prepared catalysts were identified by X-ray diffraction (XRD, Rigaku Smartlab with Cu Kα X-rays, λ= 0.15406 nm), Raman microscope (Renishaw inVia Raman, 633 nm wavelength incident laser light) and X-ray photoelectron spectroscopy (XPS, Thermo Fisher Scientific, ESCALAB 250Xi). The specific surface area and pore distribution of the as-prepared catalysts were determined with Brunauer-Emmett-Teller (BET, Quantachrome U.S.).

1.3 Electrochemical measurements:

The electrochemical performance of the as-prepared catalysts was evaluated in a conventional three-electrode system by using a Princeton Applied Research electrochemical workstation. A glassy carbon rotating desk electrode (RDE, diameter is 5 mm, area is 0.19625 cm^2) or rotating ring disk electrode (RRDE, diameter is 5.61 mm, area is 0.2475 cm^2) were used as working electrodes. A Platinum electrode and an Ag/AgCl (KCl-sat.) electrode were used as the counter and reference electrodes, respectively. To obtain homogeneous catalyst ink, 2 mg of commercial 20 wt% JM Pt/C and the as-prepared catalysts were dispersed in a 500 μL solution containing 144 μL ultrapure water, 336 μL isopropanol and 20 μL Nafion (5 wt%) solution under

sonication for 60 min. Then the catalyst film was obtained by spin coating the ink on RDE or RRDE electrode at 700 rpm for 15min at room temperature. The catalyst loading was 0.6 mg_{total} cm^{-2} for PGM-free catalysts and 0.020 mg_{Pt} cm^{-2} for Pt/C. All potentials are provided vs. reversible hydrogen electrode (RHE).

The ORR tests were conducted at 25°C in 0.1 M $HClO_4$/0.1 M KOH solution. Firstly, the catalysts were activated in Ar-saturated 0.1 M $HClO_4$/0.1 M KOH by scanning several cyclic voltammetry (CV) curves until the signals stabilized. Then the ORR activity was evaluated in O_2-saturated 0.1 M $HClO_4$/0.1 M KOH at 1600 rpm with a scan rate of 10 mV s^{-1}. Electron transfer number (n) and H_2O_2 yield was determined by RRDE measurements by holding ring electrode at 1.3 V. The n and H_2O_2% were calculated by the following equations:

$$n = 4 \times I_d / (I_d + I_r/N) \quad (1)$$

$$H_2O_2\ (\%) = 200 \times (I_r/N) / (I_d + I_r/N) \quad (2)$$

While I_d is the disk current, I_r is the ring current, and N (0.37) is the current collection coefficient of the Pt ring.

The presented ORR results were calculated by removing capacitive currents after subtracting the currents measured in Ar-saturated 0.1 M $HClO_4$/0.1 M KOH. Stability tests (accelerated durability tests (ADTs) and chronoamperometry (CA)) were conducted at 25°C in O_2-saturated 0.1 M $HClO_4$/0.1 M KOH solution by potential cycling (0.6-1.0 V, 200 mV s^{-1}, 10000 cycles) and by holding at constant potential (0.70 V), respectively.

1.4 DFT Calculations:

All the DFT calculations for spin polarization in this work are performed in the VASP Package [1]. The generalized gradient approximation (GGA) under the Perdew-Burke-Ernzerhof (PBE) generalization is used for the exchange-correlation generalization [2], and the projective suffix plus plane wave (PAW) pseudopotential method is used to describe the core electrons [3]. The empirical correction method in the Grimme scheme (DFT+D3) is used to describe the reactant or intermediate and catalyst van der Waals (vdW) interactions [4].

The catalyst was constructed by using a 6×6×1 graphene supercell as a model, while a 20 Å vacuum layer was added to eliminate the effects due to the periodic structure. The plane-wave truncated basis group truncation energy is taken as 500 eV. The Brillouin zone is sampled using 3×3×1 and 5×5×1 Monkhorst-Pack k-point grids [5] for structural relaxation and electronic structure calculations, respectively. For the electron step iteration the self-consistent field (SCF) convergence criterion is 1×10^{-5}, the frequency calculation is 1×10^{-7}, and the ion step convergence criterion is that the force on each atom is less than 0.02 eV $Å^{-1}$.

The formation energy (E_f) is calculated as:

$$E_f = E_{M\text{-}N/C} + n_C\mu_C - (E_{v\text{-}gra} + n_N\mu_N + E_{bulk}) \quad (3)$$

where $E_{M\text{-}N/C}$ is the energy of the structure after anchoring the metal atom, n_C and n_N are the number of C atoms replaced by N atoms in the catalyst and the number of nitrogen atoms, respectively, μ_C and μ_N are the chemical potentials of C and N, respectively, corresponding to the energy of a single C atom in the bulk phase graphene and the energy of a single N atom in the nitrogen, $E_{v\text{-}gra}$ is the energy of the graphene structure without the reference to N and metal atoms, and E_{bulk} is the energy of a single metal atom in the bulk phase [6].

The dissolution potential (U_{diss}) is calculated as:

$$U_{diss} = U^{\circ}_{diss} - E_f/ne^- \quad (4)$$

where U°_{diss} is the standard dissolution potential of the metal and n is the number of electrons involved in the dissolution (n=2) [7]

The adsorption energy of a reactant or intermediate is calculated by the formula

$$\Delta E_{ads} = E_{total} - (E_{adsorbate} + E_{slab}) \quad (5)$$

where E_{total}, E_{slab} and $E_{adsorbate}$ represent the energy containing the catalyst adsorbate, catalyst and adsorbate, respectively.

Nørskov et al. developed a computational hydrogen electrode (CHE) [8] model that was used to calculate the change in Gibbs free energy (ΔG) for each basic step in the ORR, calculated as

$$\Delta G = \Delta E + \Delta ZPE - T\Delta S + \Delta G_{pH} + \Delta G_U \quad (6)$$

where ΔE is the reaction energy difference of the reaction step in ORR, ΔZPE and ΔS are the change in zero-point energy and entropy at 298.15 K, which is calculated from the vibrational frequency [9]; ΔGpH is the free energy correction for pH, which is zero in this work; and $^{\Delta G_U}$ = - eU, where U is the electrode potential of the electrochemical step.

1.5 Fuel cell tests:

The Fe(***t***Co)-N-C catalyst (15 mg) was mixed with Nafion alcohol solution (5 wt%, Aldrich), isopropanol (400 mg) and deionized water (200 mg) to prepare the cathode catalyst ink, nafion : catalyst =1:1. The anode ink was made by dispersing 4 mg Pt/C (40 wt%) in the same solvent mixture as cathode catalyst ink, nafion : catalyst =1:1. The inks were subjected to sonication and stirring to make a homogeneous suspension. The catalyst ink was brushed on a piece of carbon paper (5 cm^2), followed by a drying

in a vacuum at 60°C for 4 h. The prepared cathode and anode were pressed onto the two sides of a Nafion 211 membrane (DuPont) at 130°C for 90 s under a pressure of 1.5 MPa to obtain a membrane electrode assembly (MEA). The MEA was measured by a fuel cell test station (Scribner 850e) with H_2 and O_2 (or air) at 80°C, 100% relative humidity (RH). The flow rate was 0.3 and 0.4 L min^{-1} for H_2 and O_2 (or air).

Supplementary Figures

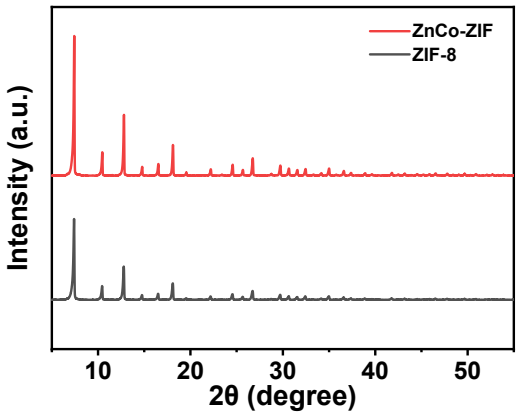

Fig. S1 XRD patterns of the Co-doped ZIF-8 (ZnCo-ZIF) precursor and ZIF-8 reference.

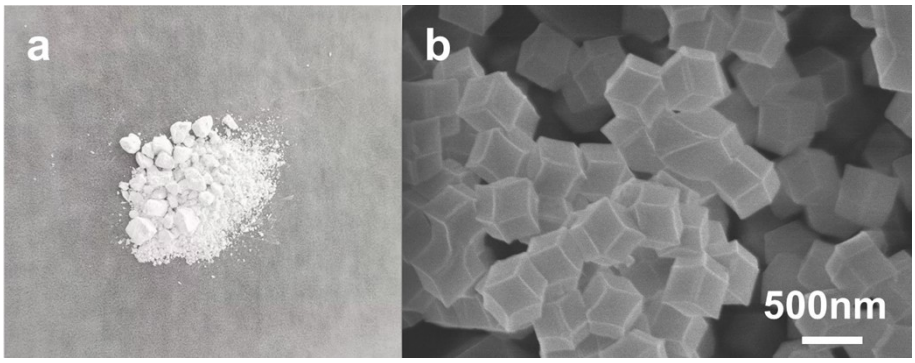

Fig. S2 The (a) powders and (b) SEM images of ZnCo-ZIF.

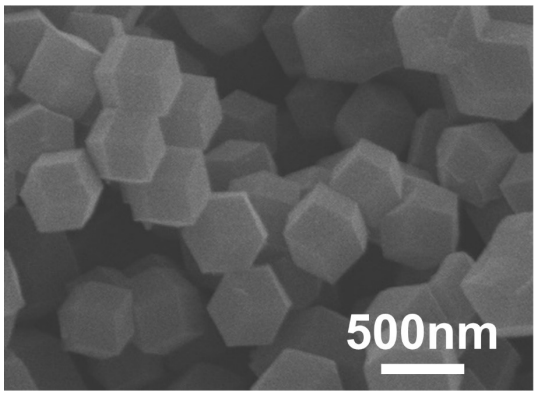

Fig. S3 The SEM images of ***t***Co-N-C (derived from the primary thermal activation of ZnCo-ZIF.

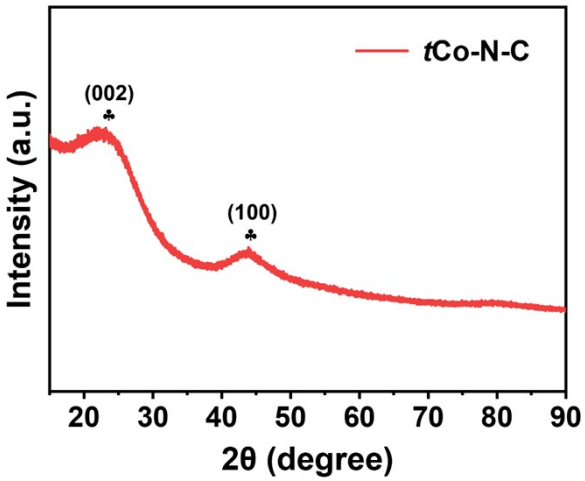

Fig. S4 XRD pattern of ***t***Co-N-C catalyst/precursor.

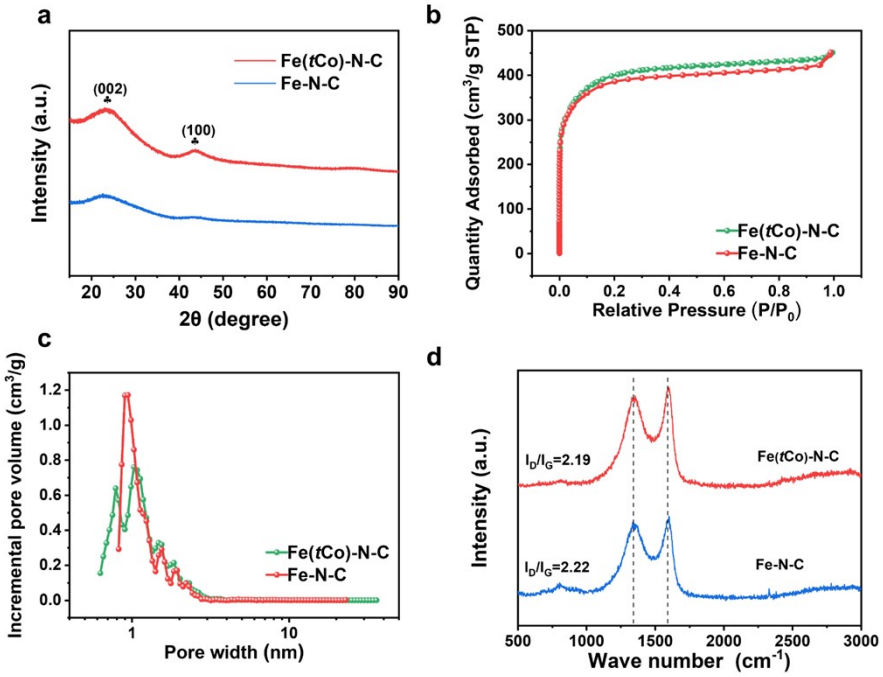

Fig. S5 (a) XRD images, (b) Adsorption desorption isotherms, (c) Pore distribution curves, (d) Raman patterns of the Fe(***t***Co)-N-C and Fe-N-C catalyst.

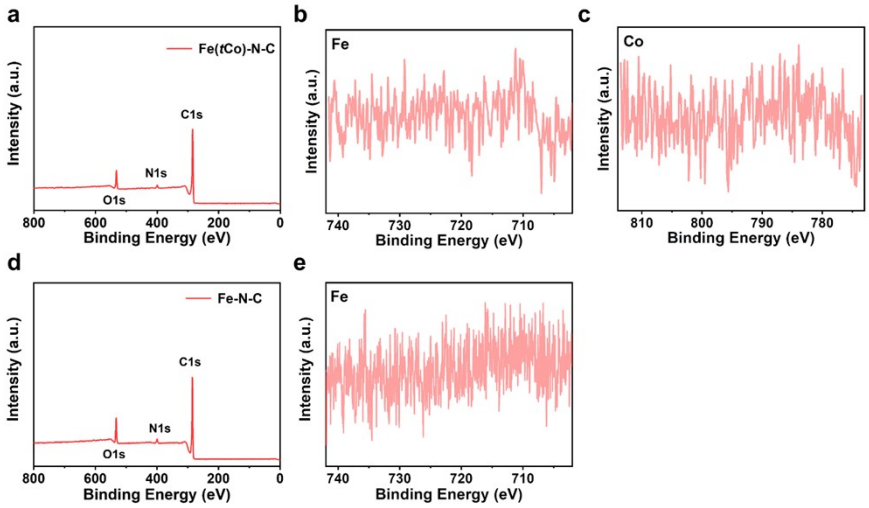

Fig. S6 (a) XPS survey, (b) High-resolution Fe 2p, and (c) High-resolution Co 2p XPS spectra for Fe(***t***Co)-N-C; (d) XPS survey, and (e) High-resolution Fe 2p for Fe-N-C.

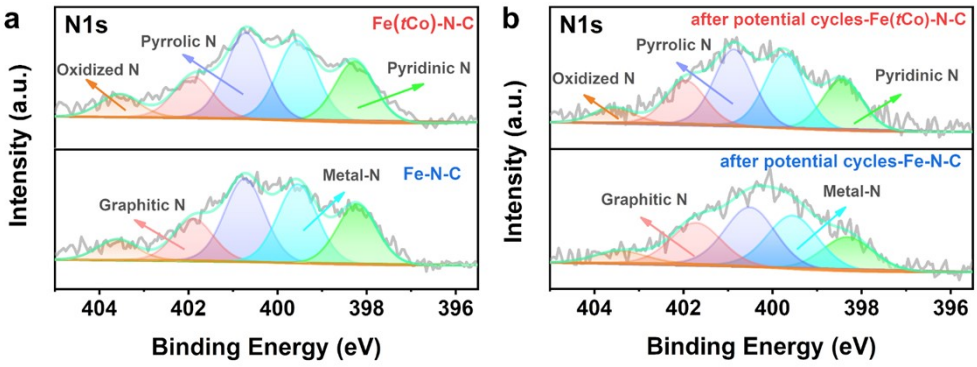

Fig. S7 High-resolution N 1s XPS results for (a) initial Fe(*t*Co)-N-C as well as Fe-N-C, and (b) the corresponding samples after 10000 CV cycles of ORR test in 0.1 M $HClO_4$ solution.

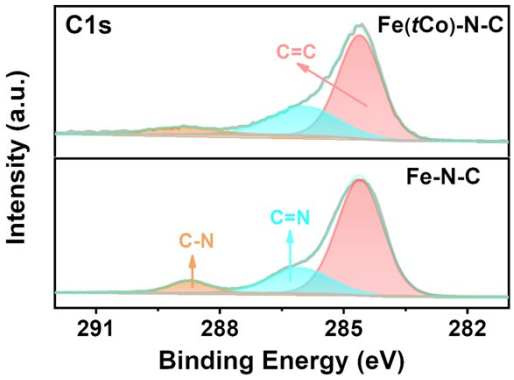

Fig. S8 High-resolution C 1s XPS results of the Fe(*t*Co)-N-C and Fe-N-C.

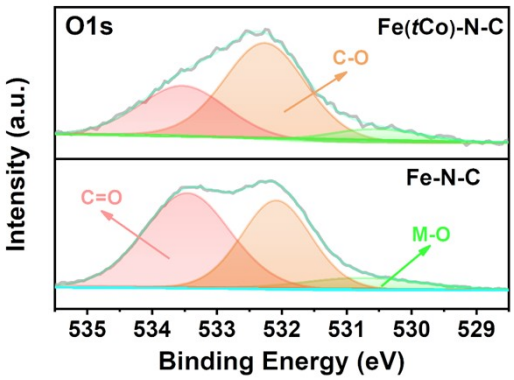

Fig. S9 High-resolution O 1s XPS results of the Fe(*t*Co)-N-C and Fe-N-C.

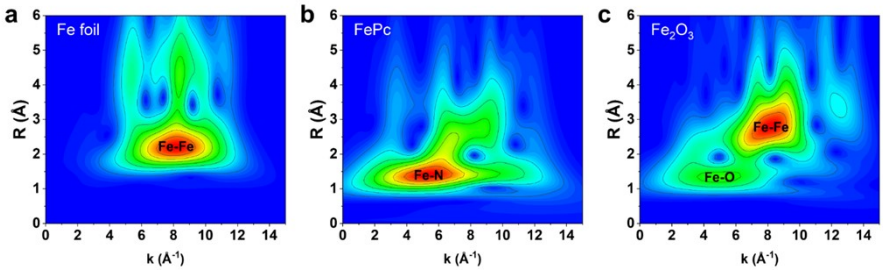

Fig. S10 k^2-weighted χ(k) k-edge WT-EXAFS spectra of (a) Fe foil, (b) FePc and (c) Fe_2O_3.

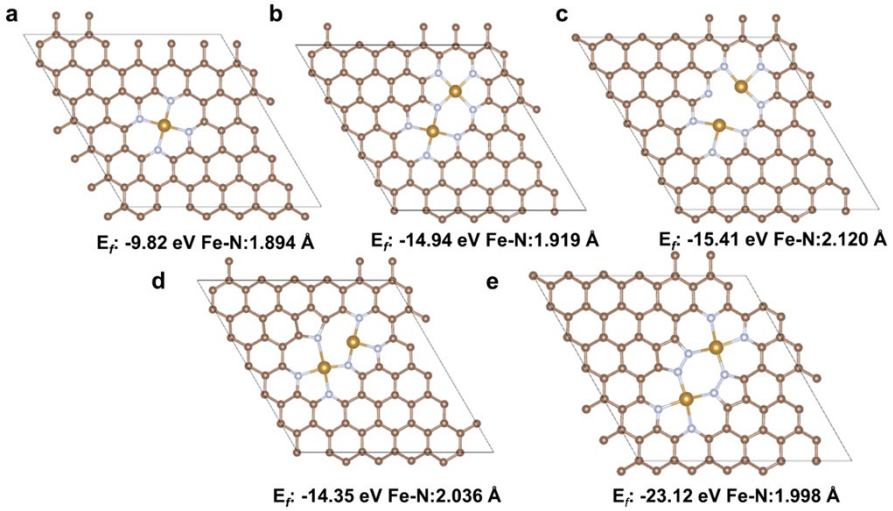

Fig. S11 The top views of (a) Fe-N_4, (b) Fe_2N_7-1, (c) Fe_2N_7-2, (d) Fe_2N_6, and (e) Fe_2N_8. The formation energies (E_f) and bond length between Fe center and adjacent N atoms (Fe-N) are presented accordingly at the bottom of each model.

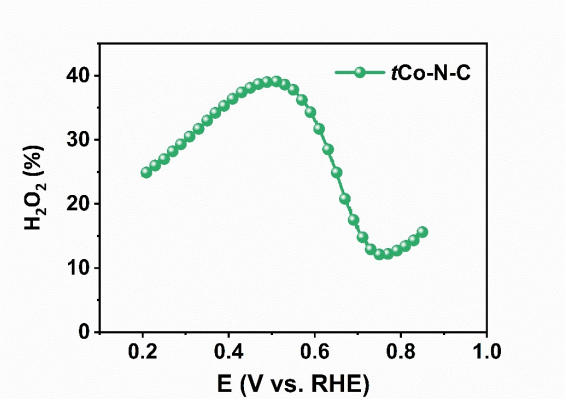

Fig. S12 H_2O_2 yield of ***t***Co-N-C in 0.1 M $HClO_4$ solution.

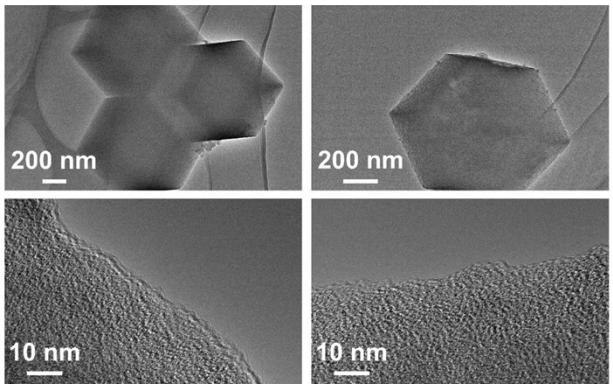

Fig. S13 TEM images of Fe(***t***Co)-N-C after 10000 CV cycles of ORR test in 0.1 M $HClO_4$ solution.

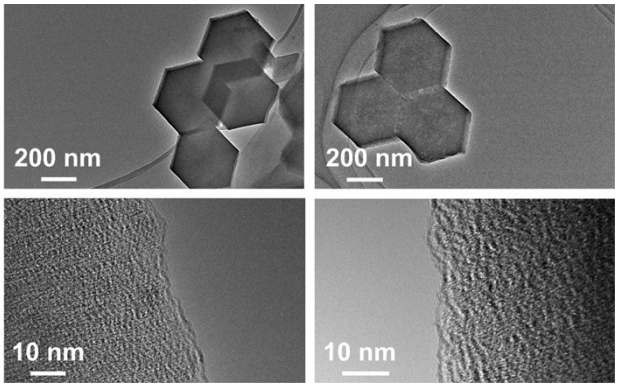

Fig. S14 TEM images of Fe-N-C after 10000 CV cycles of ORR test in 0.1 M $HClO_4$ solution.

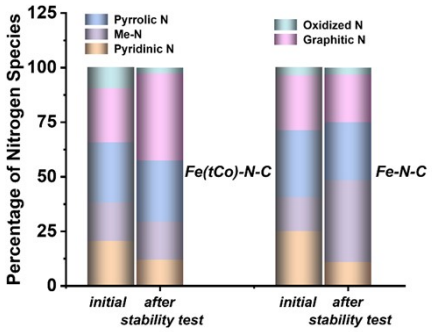

Fig. S15 Percentage of nitrogen species for Fe(***t***Co)-N-C and Fe-N-C catalysts before and after 10000 CV cycles of ORR test in 0.1 M $HClO_4$ solution.

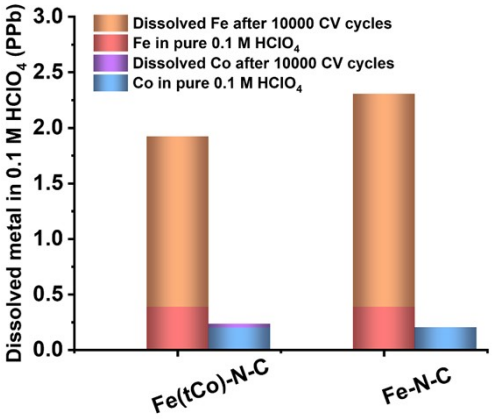

Fig. S16 Dissolved metal ion for Fe(*t*Co)-N-C and Fe-N-C after 10000 CV cycles of ORR test in 0.1 M $HClO_4$ solution detected by ICP-MS. Pure 0.1 M $HClO_4$ was also tested for reference.

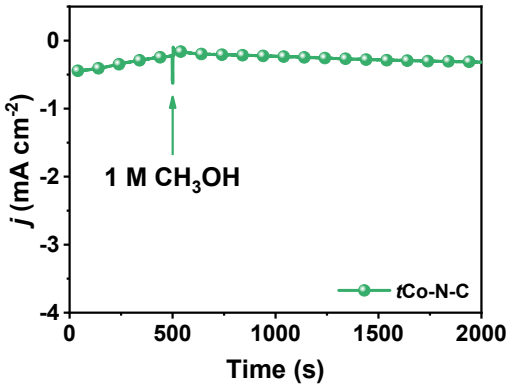

Fig. S17 Tolerance to methanol (1 M) for *t*Co-N-C in O_2-saturated 0.1 M $HClO_4$ (0.6 V, 1600 rpm).

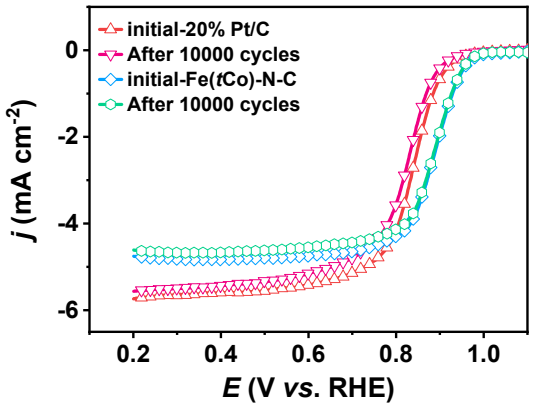

Fig. S18 Polarization LSV curves of Fe(*t*Co)-N-C catalysts and commercial Pt/C before and after 10000 cycles within 0.6-1.0 V at a scan rate of 200 mV s^{-1} in O_2-saturated 0.1 M KOH.

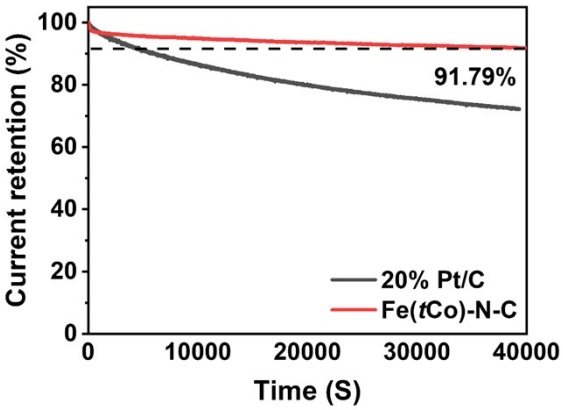

Fig. S19 Chronoamperometric tests for the Fe(*t*Co)-N-C catalysts and commercial Pt/C at 0.7 V for 40000 s in O_2-saturated 0.1 M KOH (1600 rpm).

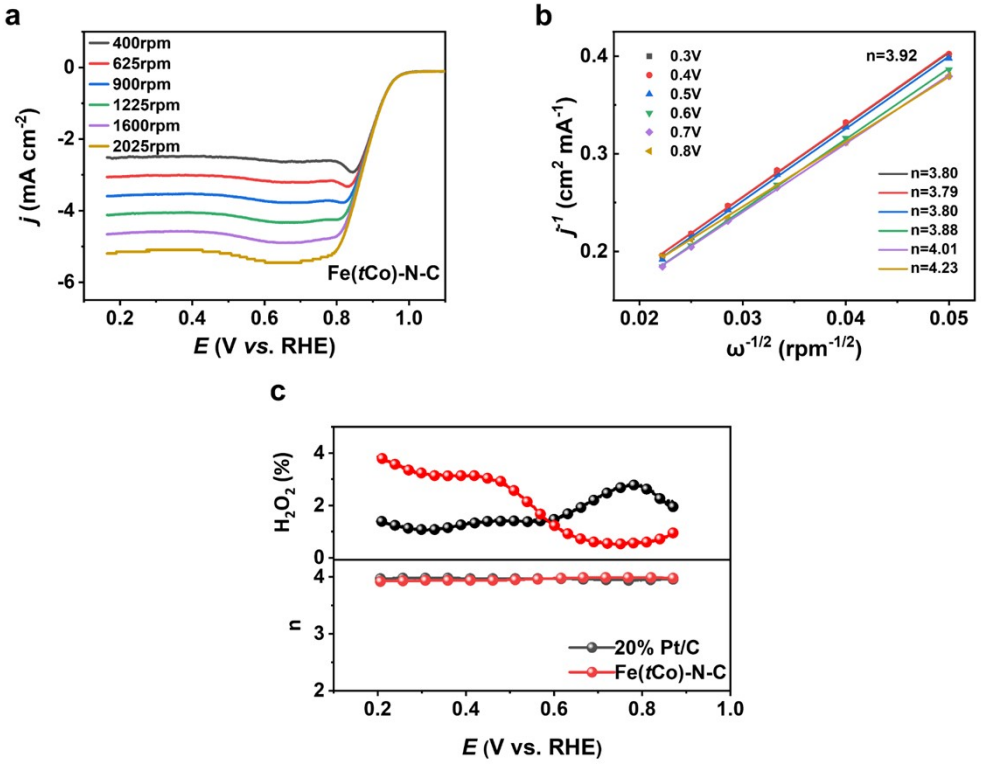

Fig. S20 (a) LSV curves at different rotating speeds, (b) the related K-L curves (0.3-0.8 V), and (c) H_2O_2 yield as well as corresponding electron transfer numbers of Fe(*t*Co)-N-C and Pt/C catalysts in O_2-saturated 0.1 M KOH.

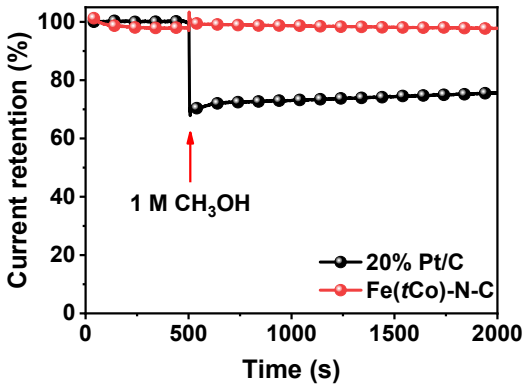

Fig. S21 Tolerance to methanol (1 M) for Fe(*t*Co)-N-C and commercial Pt/C in O_2-saturated 0.1 M KOH (0.6 V, 1600 rpm).

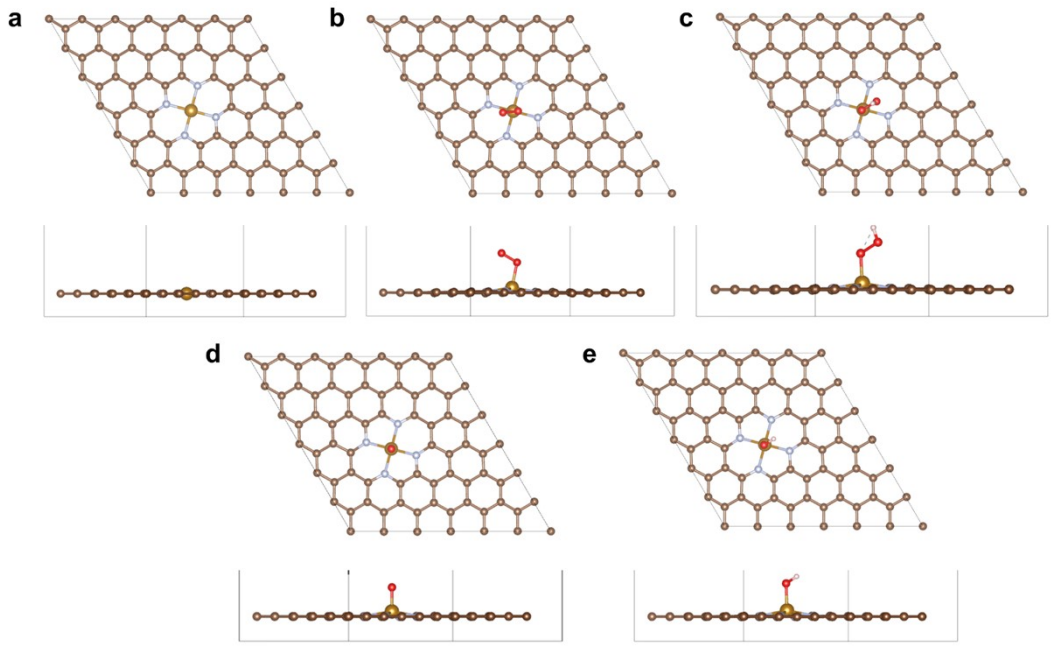

Fig. S22 The configuration of oxygenated intermediate species on Fe-N_4 sites (a) blank Fe-N_4, (b) *O_{2Fe}, (c) *OOH_{Fe}, (d) *O_{Fe}, and (e) *OH_{Fe}.

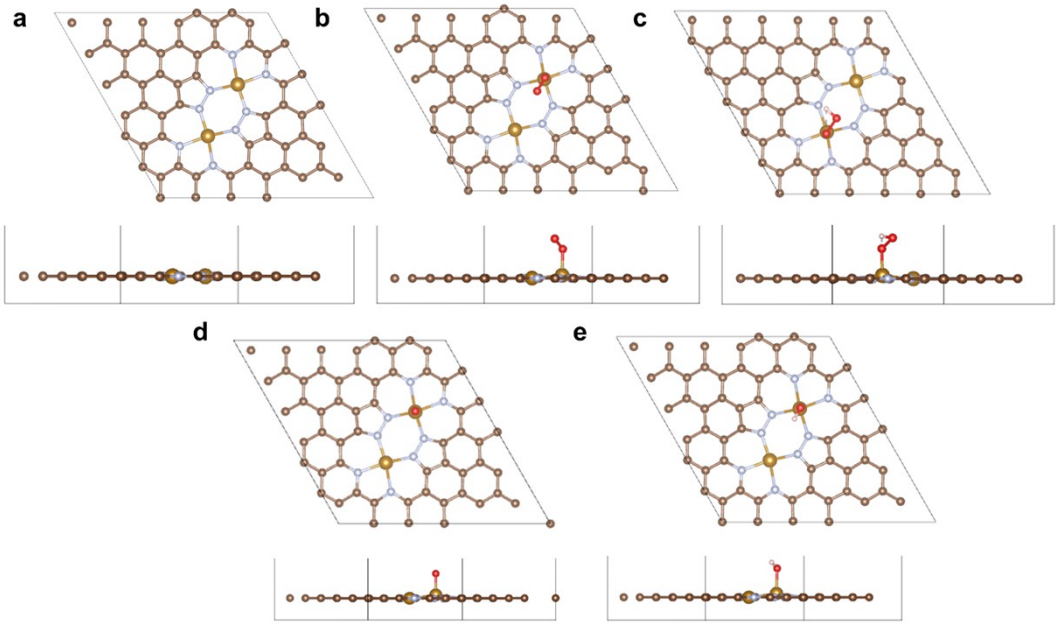

Fig. S23 The configuration of oxygenated intermediate species on Fe_2-N_8 sites (a) blank Fe_2-N_8, (b) *O_{2Fe}, (c) *OOH_{Fe}, (d) *O_{Fe}, and (e) *OH_{Fe}.

Supplementary Table

Table S1 Pore distribution and BET surface areas of the Fe(***t***Co)-N-C and Fe-N-C catalysts.

Catalyst	V_{micro}		$V_{meso\ and\ macro}$		V_{tot}	S_{BET}
	$cm^3\ g^{-1}$	%	$cm^3\ g^{-1}$	%	$cm^3\ g^{-1}$	$m^2\ g^{-1}$
Fe(***t***Co)-N-C	0.56	80.00	0.14	20.00	0.70	1486
Fe-N-C	0.55	78.57	0.15	21.43	0.70	1452

Table S2 Specific surface areas and percentage of different pore areas of the as-prepared Fe(***t***Co)-N-C and Fe-N-C catalysts.

Catalyst	S_{micro}	S_{micro}/S_{tot}	$S_{meso\ and\ macro}$	$S_{meso\ and\ macro}/S_{tot}$	S_{tot}
	$m^2\ g^{-1}$	%	$m^2\ g^{-1}$	%	$cm^2\ g^{-1}$
Fe(***t***Co)-N-C	1339	90.11	147	9.89	1486
Fe-N-C	1338	92.15	114	7.85	1452

Table S3 Elemental quantification of the as-prepared Fe(***t***Co)-N-C and Fe-N-C catalysts determined by XPS (at%).

Catalyst	C	N	O
Fe(***t***Co)-N-C	90.27%	2.79%	6.94%
Fe-N-C	91.22%	3.00%	5.78%

Table S4 Fitting results of high-resolution N 1s XPS spectra for the as-prepared Fe(***t***Co)-N-C catalysts before and after 10000 potential cycles of ORR test in 0.1 M $HClO_4$.

Catalyst	Pyridinic N	Me-N	Pyrrolic N	Graphitic N	Oxidized N
Before CV cycles	21.07%	27.60%	29.67%	13.95%	7.72%
After CV cycles	19.71%	28.53%	29.41%	16.47%	5.88%

Table S5 Fitting results of high-resolution N 1s XPS spectra for the as-prepared Fe-N-C catalysts before and after 10000 potential cycles of ORR test in 0.1 M $HClO_4$.

Catalyst	Pyridinic N	Me-N	Pyrrolic N	Graphitic N	Oxidized N
Before CV cycles	21.22%	27.62%	29.07%	14.83%	7.27%
After CV cycles	16.86%	26.63%	29.59%	20.71%	6.21%

Table S6 ICP-MS data of dissolved metal ion for Fe(***t***Co)-N-C and Fe-N-C after 10000 potential cycles of ORR test in 0.1 M $HClO_4$ (ppb).

Catalyst	Fe in 0.1 M $HClO_4$	Fe in 0.1 M $HClO_4$ after background correction	Co in 0.1 M $HClO_4$	Co in 0.1 M $HClO_4$ after background correction
Fe(***t***Co)-N-C	1.922	1.534	0.234	0.033
Fe-N-C	2.307	1.919	0.203	—

Table S7 Fe K-edge EXAFS data fitting results of the optimal Fe(***t***Co)-N-C and Fe-N-C.

Sample	Shell	*N*	*R*(Å)	$\sigma^2\times10^3$ (Å^2)	R factor (%)
Fe(***t***Co)-N-C	Fe-N	3.807±0.20	2.011	8.53	0.0060
Fe-N-C	Fe-N	3.84±0.34	1.930	11.61	0.0014

N: coordination numbers; R: bond distance; σ^2: Debye-Waller factors; R factor: goodness of fit.

Table S8 D band-center of Fe center of Fe_2N_8 and FeN_4 sites.

Active sites	Spin-Channel	d-band-center
Fe_2-N_8	Spin-UP	-2.165 eV
	Spin-DW	-0.574 eV
	Total	-1.370 eV
Fe-N_4	Spin-UP	-1.717 eV
	Spin-DW	-0.200 eV
	Total	-0.959 eV

Table S9 Comparison of ORR performance for different PGM-free catalysts in acidic media in recent years.

Catalyst	$E_{1/2}$ (vs. RHE) (1600 rpm)	Electrolyte	Catalysts loading (mg cm^{-2})	References
Fe(*t*Co)-N-C	**0.8 V**	**0.1 M $HClO_4$**	**0.6**	**This work**
HP-FeN_4	0.80 V	0.5 M H_2SO_4	0.6	Energy Environ. Sci., 2020, 13, 111
HSAC/Fe-3	0.814 V	0.5 M H_2SO_4	0.57	Adv. Sci., 2021, 8, 2002249
Fe/N/CF	0.80 V	0.5 M H_2SO_4	0.4	Proc. Natl Acad. Sci. USA, 2015, 112, 10629
(Fe,Co)/N-C	0.863 V	0.1 M $HClO_4$	0.77	J. Am. Chem. Soc., 2017, 139, 17281
Fe,Mn/N–C	0.804 V	0.1 M $HClO_4$	0.1	Nat. Commun., 2021, 12, 1734
Zn/CoN–C	0.796 V	0.1 M $HClO_4$	0.2551	Angew. Chem. Int. Ed., 2019, 58, 2622
Fe,Co/N_x/C	0.86 V	0.1 M $HClO_4$	0.4	J. Am. Chem. Soc., 2019, 141, 17763
Fe-SAs/NPS-HC	0.791 V	0.5 H_2SO_4	0.5	Nat. Commun., 2018, 9, 5422
Fe2-Z8-C	0.805 V	0.5 H_2SO_4	0.4	Angew. Chem. Int. Ed., 2018, 57, 1204-1208
TPI@Z8(SiO_2)-650-C	0.823 V	0.5 H_2SO_4	0.4	Nat. Catal., 2019, 2, 259
Fe/N/C(4mlm)-OAc	0.844 V (900 rpm)	0.1 M H_2SO_4	0.6	Adv. Funct. Mater., 2021, 31, 2009645
20Co-NC-1100	0.80 V	0.5 M H_2SO_4	0.8	Adv. Mater., 2018, 30, 1706758
20Mn-NC-second	0.80 V	0.5 M H_2SO_4	0.8	Nat. Catal., 2018, 1, 935
SA-Fe/NG	0.80 V	0.5 M H_2SO_4	0.6	Proc. Natl Acad. Sci. USA, 2018, 115, 6626
1.6%CoNC-$ArNH_3$	0.785 V	0.5 M H_2SO_4	0.5	Appl. Catal. B, 2019, 256, 117849
Co/Zn–NCNF	0.80 V	0.1 M $HClO_4$	0.6	J. Mater. Chem. A, 2020, 8, 3686
Fe SAs/N−C	0.798 V	0.1 M $HClO_4$	0.25	ACS Catal., 2019, 9, 2158
Fe-N_4-C-60	0.80 V	0.1 M $HClO_4$	0.3	Adv. Mater., 2020, 32, 2000966
0.20Mela-FeNC	~0.861 V (900 rpm)	0.1 M H_2SO_4	0.6	Energy Environ Mater., 2023, 10.1002/eem2.12611.
Fe_g-NC/Phen	0.84 V	0.1 M H_2SO_4	0.6	Energy Environ. Sci., 2022, 15, 3033.
KJ-Fe/N/Carbon	0.834 (900 rpm)	0.1 M H_2SO_4	0.6	ACS Appl. Mater. Interfaces 2022, 14, 30724.
Fe-N-C/SeO_2	0.86 V	0.5 M H_2SO_4	0.8	Adv Sci 2022, 9, 2203917.
Fe-Mn-N-C	0.79 V	0.1 M $HClO_4$	-	Appl. Catal. B Environ. 2022, 317, 121770.

Table S10 Comparison of PEMFC performance for different PGM-free catalysts under both H_2-O_2 and H_2-air atmosphere.

Catalyst	Open circuit	Peak power density (W cm^{-2})	Catalysts loading (mg cm^{-2})	References
Fe(*t*Co)-N-C	**H_2/O_2** **H_2/air**	**0.89** **0.38**	**3.0**	**This work**
HP-FeN_4	H_2/O_2	0.7	4.0	Energy Environ. Sci., 2020, 13, 111
(Fe,Co)/N-C	H_2/O_2 H_2/air	~0.85 at 0.1MPa; 0.98 at 0.2 MPa >0.505 W cm^{-2} at 0.42 V	0.77	J. Am. Chem. Soc., 2017, 139, 17281
Zn/CoN–C	H_2/O_2	0.705	—	Angew. Chem. Int. Ed., 2019, 58, 2622
Fe,Co/N_x/C	H_2/O_2	0.819	—	J. Am. Chem. Soc., 2019, 141, 17763
Fe-SAs/NPS-HC	H_2/air	0.4 at 0.40 V (80°C)	0.8	Nat. Commun., 2018, 9, 5422
Fe2-Z8-C	H_2/O_2	1.14	2.8	Angew. Chem. Int. Ed., 2018, 57, 1204-1208
TPI@Z8(SiO_2)-650-C	H_2/O_2 H_2/air	1.18 (2.5 bar H_2-O_2) 0.42	2.0	Nat. Catal., 2019, 2, 259
Fe/N/C(4mlm)-OAc	H_2/O_2 H_2/air	1.12 (1 bar)/1.33 (2 bar) 0.467 (1 bar)/0.538 (2 bar)	3.0	Adv. Funct. Mater., 2021, 31, 2009645
20Co-NC-1100	H_2/O_2 H_2/air	0.56 0.28	4.0	Adv. Mater., 2018, 30, 1706758
20Mn-NC-second	H_2/O_2	0.46 (1 bar H_2-O_2)	4.0	Nat. Catal., 2018, 1, 935
SA-Fe/NG	H_2/O_2	0.823	2.0	Proc. Natl Acad. Sci. USA, 2018, 115, 6626
1.6%CoNC-$ArNH_3$	H_2/O_2	0.826 (2.5 bar H_2-O_2) 0.305 (2 bar air)	3.0	Appl. Catal. B, 2019, 256, 117849
Co/Zn–NCNF	H_2/O_2	0.603	4.0	J. Mater. Chem. A, 2020, 8, 3686
Fe SAs/N−C	H_2/O_2 H_2/air	0.826 (2.5 bar H_2-O_2) 0.305 (2 bar air)	3.0	ACS Catal., 2019, 9, 2158
Fe-N_4-C-60	H_2/O_2	0.74	4.0	Adv. Mater., 2020, 32, 2000966
0.20Mela-FeNC	H_2/O_2 H_2/air	1.30 (2.5 bar) 0.54 (2.5 bar)	3.5	Energy Environ Mater., 2023, 10.1002/eem2.12611.
Fe_g-NC/Phen	H_2/O_2 H_2/air	1.53 (2.5 bar) 0.71 (2.5 bar)	3.5	Energy Environ. Sci., 2022, 15, 3033.
KJ-Fe/N/Carbon	H_2/O_2 H_2/air	1.28 (2 bar H_2-O_2) 1.07 (1 bar H_2-O_2) 0.66 (2 bar H_2-air) 0.59 (1 bar H_2-air)	3.2	ACS Appl. Mater. Interfaces 2022, 14, 30724.
Fe-Mn-N-C	H_2/O_2	1.048 (2.5 bar H_2-O_2)	2.0	Appl. Catal. B Environ. 2022, 317, 121770.

References

1. G. G. Kresse, and J. J. Furthmüller, Phys. Rev. B: Condens. Matter Mater. Phys., 1996, **54**, 11169-11186.
2. J. P. Perdew, K. Burke and M. Ernzerhof, Phys. Rev. Lett., 1996, **77**, 3865-3868.
3. P. E. Blochl, C. J. Först, J, Schimpl, Phys. Rev. B: Condens. Matter Mater. Phys., 1994, **50**, 17953-17979.
4. S. Grimme, J. Comput. Chem., 2006, **27**, 1787-1799.
5. H. J. Monkhorst, J. D. Pack, Phys. Rev. B, 1976, **13**, 5188-5192.
6. Y. L. Sun, J. Wang, Q. Liu, M. R. Xia, Y. F. Tang, F. M. Gao, Y. L. Hou, J. Tse, Y. F. Zhao, J. Mater. Chem. A, 2019, **7**, 27175-27185.
7. X. Y. Guo, J. X. Gu, S. R. Lin, S. L. Zhang, Z. F. Chen, S. P, Huang, J. Am. Chem. Soc., 2020, **142**, 5709-5721.
8. J. K. Nørskov, J. Rossmeisl, A. Logadottir, L. Lindqvist, J. R. Kitchin, T. Bligaard, H. Jónsson, J. Phys. Chem. B, 2004, **108**, 17886-17892.
9. V. Wang, N. Xu, J. C. Liu, G. Tang, W. T. Geng, Comput. Phys. Commun., 2021, **267**, 108033.
10. X. P. Han, X. F. Ling, Y. Wang, T. Y. Ma, C. Zhong, W.B.Hu, Y. D. Deng, Angew. Chem. Int. Ed., 2019, **58**, 5359-5364.
11. J. Z. Li, H. G. Zhang, W. Samarakoon, W. T. Shan, D. A. Cullen, S. Karakalos, M. J. Chen, D. M. Gu, K. L. More, G. F. Wang, Z. X. Feng, Z. B. Wang, G. Wu, Angew. Chem. Int. Ed., 2019, **58**, 18971-18980.
12. Y. H. He, Q. R. Shi, W. T. Shan W, X. Li, A. J. Kropf, E. C. Wegener, J. Wright, S. Karakalos, D. Su, D. A. Cullen, G. F. Wang, D. J. Myers and G. Wu, Angew. Chem. Int. Ed., 2021, **60**, 9516-9526.
13. Y. Y. Qiao, P. F. Yuan, Y. F. Hu, J. N. Zhang, S. C. Mu, J. H. Zhou, H. Li, H. C. Xia, J. He and Q. Xu, Adv. Mater., 2018, **30**, 1804504.
14. Y. Y. Liang, Y. G. Li, H. L. Wang, J. G. Zhou, J. Wang, T. Regier and H. J. Dai, Nat. Mater., 2011, **10**, 780-786.
15. Y. R. Li, S. H. Yin, L. Chen, X. Y. Cheng, C. T. Wang, Y. X. Jiang, S. G. Sun, Energy Environ. Mater., 2023, 10.1002/eem2.12611.
16. S. H. Yin, S. L. Yang, G. Li, G. Li, B. W. Zhang, C. T. Wang, M. S. Chen, H. G. Liao, J. Yang, Y. X. Jiang, S. G. Sun, Energy Environ. Sci., 2022, **15**, 3033-3040.
17. P. Y. Zhang, X. H. Yang, Q. R. Jiang, P. X. Cui, Z. Y. Zhou, S. H. Sun, Y. C.

Wang, S. G. Sun, ACS Appl. Mater. Interfaces., 2022, **14**, 30724-30734.